Irradiation-tolerant Nanostructured Ferritic Alloys: Transforming Helium from a Liability to an Asset

G.R. Odette and D.T. Hoelzer

Nanostructured ferritic alloys (NFAs) have the potential to make transformational contributions to developing advanced sources of fission and fusion energy. NFAs are Fe-Cr based ferritic stainless steels that contain an ultrahigh density of Y-Ti-O nanofeatures (NFs). The NFs provide both outstanding high temperature properties and remarkable tolerance to irradiation induced displacement damage as well as the degrading effects of transmutation product helium. Indeed, NFs can transform helium from a liability to an asset by forming a high density of nm-scale bubbles that act as sinks for point defects and helium may provide near immunity to radiation damage. This article outlines recent progress on engaging the challenges facing NFA development.

INTRODUCTION

The compelling need to reduce reliance on fossil fuels while meeting rapidly growing energy demand has stimulated worldwide interest in advanced fission and fusion energy. The viability of nuclear energy will ultimately depend on developing new, high performance structural materials that can support extended component lifetimes under extremely hostile conditions, characterized by combinations of high temperatures, large time-varying stresses, chemically aggressive environments, and intense neutron radiation fields.[1,2]

The challenges presented by irradiation effects are particularly daunting. High-energy neutrons displace large numbers of atoms from their lattice positions, creating excess concentrations of vacancy and self-interstitial atom (SIA) defects. Lifetime goals for some reactor components may require tolerance of up to 400 displacements-per-atom (dpa). Nuclear n,α reactions also generate insoluble helium. These primary damage sources interact to drive complex microstructural and microchemical evolutions, which, in turn, typically degrade a host of performance sustaining material properties.[1,2] Predicting complex irradiation effects is very difficult, in part because they depend on the combination of many irradiation (temperature, dpa, dpa rate and helium/dpa ratio) and material (composition and microstructure) variables.

Our objective is to review the status of a new class of materials that we call nanostructured ferritic alloys (NFAs). Nanostructured ferritic alloys derive from oxide dispersion strengthened (ODS) steels, like PM2000.[2] They manifest high tensile, creep, and fatigue strengths, unique thermal stability, and remarkable irradiation tolerance. The outstanding characteristics of NFAs result from the presence of an ultrahigh density of Y-Ti-O rich nanofeatures (NFs). The multifunctional NFs impede dislocation climb and glide, enhance SIA-vacancy recombination and, perhaps most importantly, trap helium in small, high-pressure gas bubbles. The bubbles reduce the amount of helium reaching grain boundaries, thus avoiding severe toughness loss at lower irradiation temperatures, and potential degradation of creep rupture properties at higher temperatures. In principle, helium trapped in a high number density of small bubbles also mitigates many other manifestations of irradiation effects, including void swelling.

However, NFAs are in the very early stages of development. Important challenges and opportunities they face include: (a) determining the structures of the NFs and their interface with the ma-

How would you…

…describe the overall significance of this paper?

Nanostructured ferritic alloys show great promise of high performance and unprecedented radiation damage tolerance that will be critical to developing advanced fission and fusion energy. This paper emphasizes the critical role of nanometer-scale Yi-Ti-O precipitates in providing these remarkable attributes, including the potential for the nanofeatures to transform helium from a liability to an asset. The challenges facing the developing nanostructured ferritic alloys are reviewed.

…describe this work to a materials science and engineering professional with no experience in your technical specialty?

Energetic fission and fusion neutrons create self-interstitial and vacancy defects, and generate insoluble helium. The helium and defects lead to complex microstructural evolutions that degrade a host of properties. Nanostructured ferritic alloys contain an ultra-high density of nm-scale Y-Ti-O precipitates that provide high temperature creep strength, enhance the self-healing of the defects and trap helium in fine scale, harmless interface bubbles that could lead to near immunity to radiation damage.

…describe this work to a layperson?

Intense neutron bombardment causes severe damage to alloys in nuclear reactors by breaking down their beneficial internal structures and by injecting helium atoms that can make materials swell and become brittle. A new type of alloy is being developed that uses nanoparticles, only about one tenth of a millionth of an inch in diameter, to provide ultra-high strength and resistance to, and possibly near immunity to, neutron damage.

trix, as well as their compositions, that is their 'character;' (b) relating the NF characteristics to their ability to provide sustained high temperature strength and irradiation tolerance; (c) demonstrating and understanding the thermal and irradiation stability of far-from-equilibrium NFs and NFA microstructures; (d) identifying alloy composition-synthesis designs and thermal mechanical processing paths that optimize the NFs, and the balance of NFA microstructures, so as to provide a balanced suite of outstanding and isotropic properties; and, (e) developing practical fabrication and joining methods that preserve optimal NFA microstructures and yield defect-free components. Other practical NFA challenges include reducing costs, improving alloy homogeneity and reproducibility, establishing industrial scale supply sources and qualifying new alloys for nuclear service.

IRRADIATION EFFECTS AND TOLERANCE: THE ROLE OF HELIUM BUBBLES

Void swelling illustrates how displacement damage and helium can combine to drive the many scourges of irradiation effects. For simplicity, we consider swelling in a single-phase Fe-Ni-Cr austenitic stainless steel model alloy and use elementary rate theory to show that helium bubbles can either exacerbate or mitigate swelling, as well as other manifestations of irradiation effects. A few examples of a large literature on helium effects[2,3–8] are summarized in what follows. Note that in order to limit the references, Reference 2 (2008), which reviews the various topics and contains the pertinent specific citation, will be instead used here.

Figure 1 schematically illustrates key radiation damage processes. Fast neutron reactions create a spectrum of primary recoiling atoms with energies ranging from less than one up to several hundred keV. The primary recoils produce a branching cascade of multiple generations of additional recoiling atoms that displace atoms from their crystal lattice sites, creating equal numbers of vacancy and self-interstitial atom (SIA) defects (Figure 1a). The dose unit for this form of radiation damage is dpa. The fates of the primary defects include recombination of vacancies and SIA (Figure 1b), annihilation at various sinks (Figure 1b,d) and aggregation to form SIA dislocation loops (Figure 1c), and vacancy clusters or growing voids (1e). Nuclear (n,α) reactions also generate helium.

Voids typically do not homogeneously nucleate at reactor dpa rates, but rather form on helium bubbles (Figure 1d,e,f). Thus helium bubbles are a prerequisite to void swelling. Helium is insoluble and quickly clusters to form bubbles. The bubble number densities (N_b) and sizes (r_b) depend on many irradiation and material variables. The bubbles are stable and grow with the addition of helium atoms (m) up to a critical gas content, m*, where they convert to unstably growing voids (Figure 1d,e,f). The critical m* is proportional to $\ln(\phi)^{-2}$, where ϕ is an effective vacancy supersaturation (>1) that results from the preferential annihilation of SIA at dislocations (Figure 1c), leaving an excess flux of irradiation-induced vacancies at other sinks (Figure 1b,d,e).

The vacancy supersaturation is controlled by the strengths (Z) of various defect sinks, a dislocation bias factor for SIA (B) and the vacancy generation rate. In the simplest case the sinks are composed of bubbles ($Z_b \approx 4\pi r_b N_b$), dislocations ($Z_d \approx \rho$ for vacancies and $Z_{di} = (1 + B)\rho$ for SIA) and voids ($Z_v \approx 4\pi r_v N_v$). Here, ρ is the dislocation density, while N_v and r_v are void number density and radius, respectively. The excess vacancy flux to smaller bubbles is exactly balanced by vacancy emission due to the Gibbs–Thompson capillary effect (Figure 1d,f). However, vacancies accumulate in larger growing voids, with lower emission rates, resulting in bulk swelling at a rate $\dot{S}$, defined as the fractional volume increase per dpa (Figure 1g). Cavity microstructures may consist of: voids (converted from bubbles), bubbles (that remain smaller than m*), or a bimodal distribution of small bubbles and larger voids.

Figure 2a shows the effect of Z_b/Z_v on the post-incubation $\dot{S}$ as a function of Z_v/Z_d. If all the bubbles convert to voids, $\dot{S}$ is maximum when N_v (equal to the pre-incubation N_b) increases up to the point where $Z_v \approx Z_d$. However, if $Z_v > Z_d$, $\dot{S}$ decreases with further increases in N_v. $\dot{S}$ is further reduced by the Z_b from any bubbles that do not convert to voids. Indeed, $\dot{S}$ scales as $1/N_b^2$ in a bubble sink dominated microstructure, with $Z_b >> Z_v \approx Z_d$ (Figure 1i).

The combination of m* and N_b control the incubation dose (dpa_i) prior to the onset of void swelling. Assuming all the helium goes to a single size class of N_b bubbles, dpa_i scales with $N_b m^*$. That is, the incubation dpa_i increases with the number and helium content of the critical bubbles. Figure 2b shows the effect of N_b on dpa_i for parameters typical of an austenitic stainless steel taken from Reference 5 in the peak swelling temperature regime. Note this calculation ignores recombination and the effects of cascade vacancy cluster sinks, resulting in an underestimate of the dpa_i at low N_b; however, the predicted trends are qualitatively correct. The dpa_i initially increases in direct proportion to N_b, but, in the bubble sink dominated regime, approaches a limiting scaling of N_b^5.

Thus there are competing effects of increasing the number of bubbles, and at higher dpa >> dpa_i, swelling peaks at an intermediate N_b. More notably, however, even a moderately high number of bubbles can lead to a very large increase in dpa_i, potentially completely suppressing void swelling, as suggested by the dashed line in Figure 2b at 400 dpa. Bubbles are also extremely deep traps and efficient reservoirs for helium stored at capillary pressures of $\approx 2\gamma/r_b$.

A similar divide and conquer strategy is pertinent to high-temperature helium embrittlement which is due to stress driven growth of creep cavities that convert from grain boundary bubbles after they have grown to m*.[7] The resulting degradation of creep properties can also be mitigated by a high number of small grain boundary bubbles that maintain m << m*. Matrix bubbles also reduce the amount of helium reaching grain boundaries. Note that protecting grain boundaries is also important at lower irradiation temperatures in tempered martensitic steels (TMS), where helium accumulation can result in an enormous enhancement of brittle to ductile transition temperature shifts and intergranular fracture paths.[2] More generally, high N_b suppresses swelling and many other manifestations of irradiation effects.

However, some caveats are in order. First, the bubbles themselves can

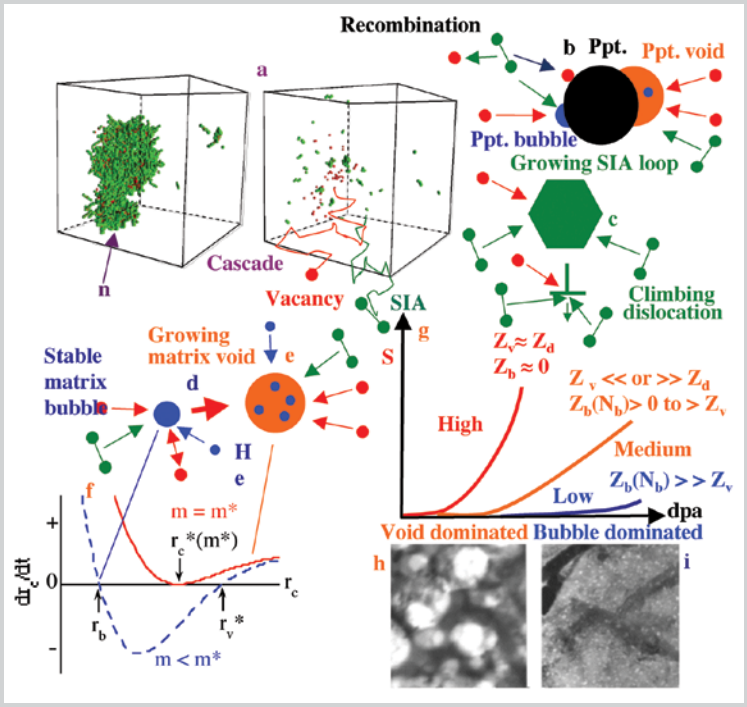

Figure 1. Pictorial illustrations showing the basics of how helium and displacement damage interact in a way that can lead to void swelling.

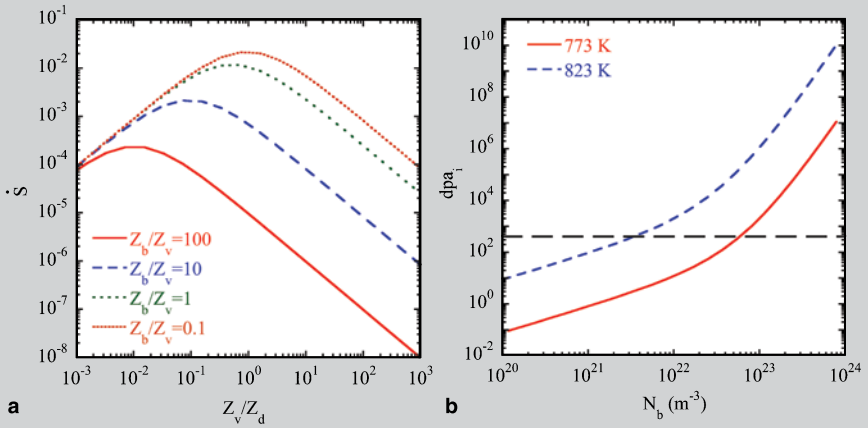

Figure 2. (a) Swelling rate ($\dot{S}$) as a function of the void to dislocation sink strength ratio (Z_v/Z_d) for various bubble to void sink strength ratios (Z_b/Z_v) showing that either too few, or too many, bubbles suppress swelling; and (b) prediction showing that even a moderate number density (N_b) of 1 nm helium bubbles could increase the incubation dose for swelling (dpa_i) to more than 400 dpa shown by the horizontal dashed line.

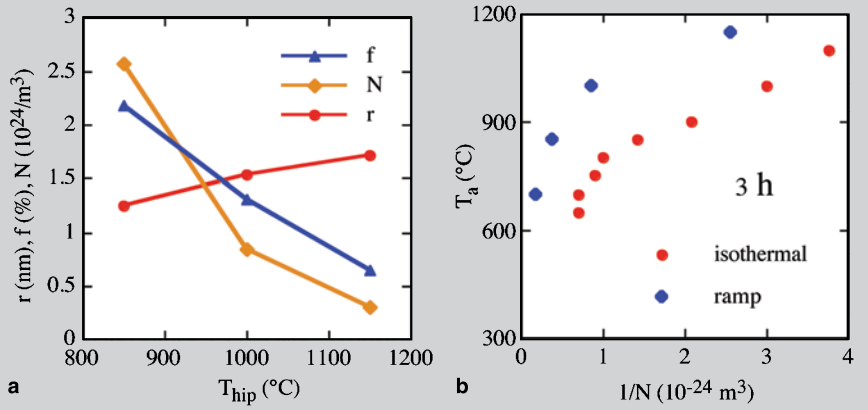

Figure 3. (a) The variation of the NF N, r, and f in a model 14CrYWT showing an effect of HIPing temperature that is consistent with expectations for precipitation of the Y-T-O features; and (b) 1/N as a function of the annealing temperatures for 14CrYWT model alloy powders showing C-curve type kinetics above a nose around 650°C.

cause hardening, but when they are associated with NFs the increment is not expected to be large. Second, it has been observed that at lower irradiation temperatures, small dislocation loops, that can also cause hardening and may act as segregation-precipitation sites, form even in the presence of a high concentration of bubbles.[6] However, NFA are capable of operating at higher irradiation temperatures, above the displacement damage regime, where rapid recovery (self-healing) prevents such defect accumulation. More generally, the degree to which an NF-bubble dominated microstructure suppresses various types of irradiation effects remains to be quantified.

The concepts outlined above underscore the importance of the helium/dpa ratio.[3,5,6] In the case of austenitic stainless steels irradiated in fast reactors the helium/dpa ≈ 0.2 appm/dpa is sufficient to form a population of bubbles that almost all convert to voids, leading to rapid swelling. Thermal neutron n_{th},α reactions with the nickel contained in austenitic stainless steels irradiated in mixed spectrum reactors produce high helium/dpa ≈ 50 appm/dpa, leading to large N_b that can sometimes suppress swelling.[3,5,6] There is evidence that an intermediate helium/dpa ≈ 10 appm/dpa, characteristic of fusion neutron spectra, may cause peak swelling in some cases. The simple picture drawn here is modified in other alloys, such as 9Cr TMS that have more complex microstructures and are more swelling resistant for a variety of reasons, including having a low helium/dpa < 0.1 appm/dpa in fast reactors due to the absence of Ni.[8] However, the higher fusion helium/dpa might result in significant swelling in TMS at high dpa (see the sidebar).

In summary, for conditions that lead to low to intermediate N_b, voids and creep cavities can form after an incubation period associated with helium driven growth of bubbles to m*. In this case the alloys are generally vulnerable to swelling and many other manifestations of irradiation effects. However, very high N_b, with m << m*, would provide, in principle, significant and persistent protection against irradiation effects of many types over a wide range of temperatures up to several hundred

dpa and very high helium concentrations.

High bubble densities can be achieved by trapping helium on the interfaces of fine scale precipitates, such as carbide, nitride and phosphide phases.[2,6] However, to be effective, the precipitates must be stable under irradiation, which is not always the case, especially at higher temperatures. In addition to their thermal stability, the ability of precipitates to form fine scale helium bubbles is expected to depend on: their number density, size distribution, and total sink strength; and their interface structure

IN-SITU HELIUM IMPLANTATION STUDIES

In-situ helium implantation in mixed spectrum fission reactor irradiations provides an attractive approach to assessing the effects of helium-dpa synergisms.[2,9,10] The idea is to use Ni (or B or Li)-bearing implanter layers to inject high-energy α-particles into an adjacent material that is simultaneously undergoing fast neutron induced displacement damage. The α-particles can be produced by two-step $^{58}Ni(n_{th},\gamma)^{59}Ni(n_{th},\alpha)$ thermal neutron (n_{th}) reactions. A series of in-situ helium implantation irradiation experiments were recently carried out in the mixed spectrum high flux isotope reactor (HFIR). Micrometer scale NiAl injector coatings were used to uniformly implant α-particles to a depth of ≈ 5 to 8 μm in transmission electron microscopy (TEM) discs for a large matrix of alloys irradiated over a wide range of temperatures and dpa at controlled helium/dpa ratios ranging from << 1 to 40 appm/dpa. Here we compare the cavity structures in a 14Cr NFA, MA957, to those in an 8Cr TMS, F82H, following HFIR irradiation at 500°C to 9 dpa and 380 appm helium. The experimental details are given elsewhere.[9,10]

Through-focus sequence TEM images were used to characterize the bubbles, with care taken to avoid surface artifacts. Bubble-like features were generally not found in the unimplanted regions of either MA957 or F82H. As illustrated in a typical under-focused image in Figure Aa, a high number density ($N_b \approx 4.3\times10^{23}/m^3$) of very small (average $d_b \approx 1.3$ nm) bubbles were observed in the NFA. The inserts in Figure Aa show examples of the decoration of larger features with cavities. Image overlap analysis suggests that most bubbles are associated with a similar number density (≈ $6.5\times10^{23}/m^3$) of NFs.[2,10] However, the degree of bubble-NF association has not yet been fully demonstrated and quantified. The boundary in MA957 in Figure Aa appears to be relatively cavity free, and there does not seem to be a large nearby NF-cavity denuded zone. Assuming equal partitioning of all the 380 appm helium to $4.3\times10^{23}/m^3$ bubbles (≈ 70 helium atoms/bubble) and $\gamma = 2$ J/m² is consistent with $r_b \approx 2\gamma/zmkT \approx 1.3$ nm at 500°C, where z is the real gas compressibility factor, which is in remarkable agreement with the measured average cavity size. Thus we conclude that the helium is primarily stored in near-equilibrium bubbles at a capillary pressure of $2\gamma/r_b \approx 2{,}670$ MPa in this case. A higher helium content of 2,000 appm partitioned to the same number of bubbles (≈ 370 helium atoms/bubble) increases r_b to ≈2.2 nm, still far below the critical size for void formation, which is estimated to be well over 10 nm. The 9 dpa irradiation at 500°C has no observable effect on the NFs.

As shown in Figure Ab, a lower number density of ($N_b \approx 5.3\times10^{22}/m^3$) of somewhat larger ($d_b \approx 2.8$ nm) bubbles (the smaller population of cavities in this case) are observed in F82H, along with much larger faceted cavities, that are likely voids.[2,9] The smaller matrix bubbles in F82H are clearly formed on dislocations, as highlighted by the black and white contrast insert in Figure Ab. Figure Ac shows the cavity size distribution is much narrower in the MA957, with a maximum diameter of less than 2.5 nm. In contrast, the largest diameters exceed 10 nm in F82H and it appears that a bimodal bubble-void cavity size distribution is developing.[2,9,10] Model based extrapolation of these results suggests that significant swelling may develop at higher helium and dpa.

The in-situ helium implantation results suggest that NFs are effective in trapping helium in fine scale bubbles at least up to 500°C. The sink strength of $4.3\times10^{23}/m^3$, 1.3 nm bubbles is $Z_b \approx 3.5\times10^{15}/m^2$, which is significantly higher than the typical total sink strength in TMS alloys ($< \approx 10^{15}/m^2$). Presumably, Z_b could be increased by an additional factor of at least 2 to 3 in alloys with larger numbers of NFs and larger associated bubbles at higher helium levels.

It is important to emphasize that both helium bubbles and NFs are key to highly irradiation tolerant alloys. The primary role of the NFs is to provide preferred sites for forming bubbles. Helium management schemes based on these principles are critical to developing fusion energy, and may also play a role in fission applications intended to reach very high dpa levels. The effect of helium bubbles on defect damage accumulation is being investigated using the in situ implantation technique, including at higher helium and dpa, for a wide range of irradiation temperatures and a large alloy matrix.

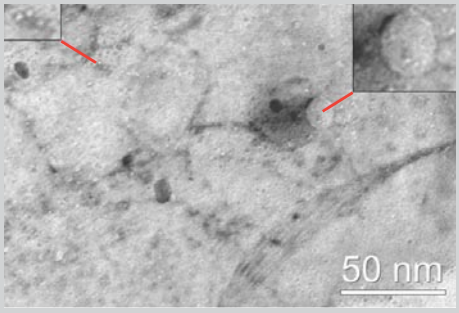

a

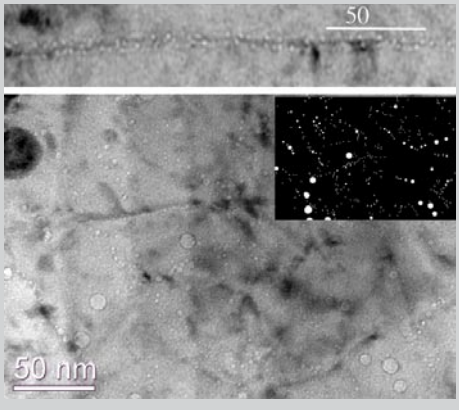

b

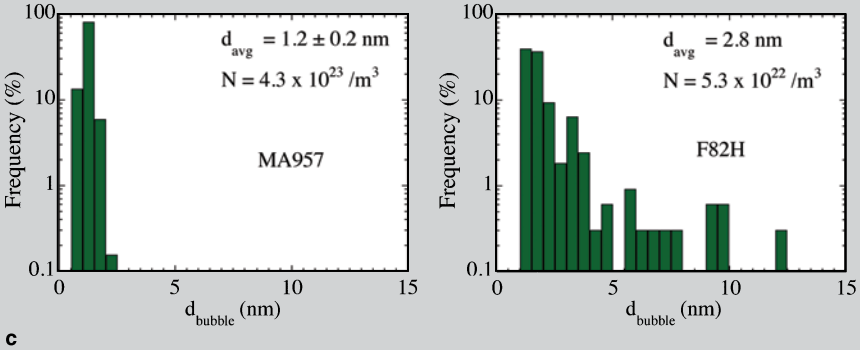

c

Figure A. (a) TEM image of in situ helium injected MA957 showing many small bubbles; (b) TEM image of in-situ helium injected F82H showing a lower number density of cavities including both small dislocation-associated bubbles (see insert) and larger voids (The thin miocrograph on the top of Figure Ab shows an interface that is highly decorated with bubbles); and (c) the corresponding cavity size distributions.

and elastic properties. Large numbers of thermally stable NFs that effectively trap helium would be optimal. However, the idea of stable, yet far from equilibrium, NFs has the ring of being an oxymoron from the perspective of near equilibrium materials science. As discussed in the sidebar on in-situ helium implantation studies, however, NFs may contradict this conventional wisdom.

NFA PROCESSING AND NF PRECIPITATION KINETICS

We focus here on Fe-14Cr-1-3W alloys micro-alloyed with Ti, Y, and O solutes that are the primary constituents of the NFs.[2] Nanostructured ferritic alloys are typically processed by ball milling pre-alloyed, rapidly-solidified metal powders and yttria (Y_2O_3) oxide powders.[2] Proper milling effectively dissolves the Ti, Y, and O solutes that then precipitate as NFs during hot consolidation. Powder consolidation is usually followed by a series of deformation processing treatments.

The number density (N), size (r) distribution, and volume fraction (f) of the NFs primarily depend on the processing temperature history and the alloy composition.[1,12] Figure 3a shows the N, r, and f measured by small angle neutron scattering (SANS) in a 14Cr-0.4Ti-3W-0.25-Y_2O_3 (14CrYWT) model alloy as a function of the HIPing temperature.[2,12] As expected, r increases, while the N and f decrease, with increasing temperature. Figure 4b shows 1/N as a function of temperature in mechanically alloyed powders that were either ramp annealed, to mimic the HIP cycle, or isothermally annealed, which is closer to extrusion conditions; the annealing time was 3 h in both cases. Quasi C-curve time-temperature precipitation kinetics is observed. The ramp-anneal produces a higher N, due to longer time spent at lower temperatures, compared to the isothermal annealing treatment. Isothermal anneals over a range of times showed that NF precipitation is rapid at temperatures above ≈600°C. These studies also demonstrated that Ti is necessary to form NFs at higher consolidation temperatures. The SANS r, N, and f data are broadly consistent with the results of other characterization methods including a variety of TEM techniques and atom probe tomography (APT).[11]

THE CHARACTER OF THE NFs

Optimizing NFAs requires understanding of the detailed composition and structure of the NFs, as well as how alloying elements and processing variables affect their character. While it is clear that a suite of characterization tools is needed to develop such understanding, various techniques are not yet fully consistent with one another. The equilibrium phases in the Y-Ti-O system are cubic pyrochlore $Y_2Ti_2O_7$ and orthorhombic Y_2TiO_5 complex oxides (other oxides include $YTiO_3$ and YTi_2O_6).[2] Some transmission electron microscopy (TEM) and x-ray diffraction (XRD) studies have previously identified $Y_2Ti_2O_7$ and Y_2TiO_5 in NFAs,[2,13] but generally for feature diameters of 5 nm or more. The magnetic to nuclear scattering (M/N) ratios measured in SANS studies can be compared to corresponding calculated values for specified phases with known compositions and atomic densities.[12] The observed M/N ranged from slightly less than 1 to more than 2, compared to values of about ≈1.3–1.4 for the complex oxides. Lower values are associated with processing the milled powders at higher average temperature. Given the uncertainties in measuring and interpreting M/N the SANS data are broadly consistent with somewhat non-equilibrium oxide compositions and atom densities.

Atom probe tomography (APT) data also suggest that the NFs are non-stoichiometric, perhaps coherent sub-oxide transition phases, or zones.[2] Figure 4 shows an example of an enlarged atom image of an NF (Figure 4a), along with an iso-composition (Y plus Ti > 3%) reconstruction of NFs in MA957 (Figure 4b).[11] APT compositions consistently show much higher Ti/Y ratios, typically ≈1.5–4/1, and low O/[Ti + Y] ratios—<1.[2,11,14] These values differ from those for the equilibrium oxides, with Ti/Y of 0.5 to 1 and O/[Ti + Y] = 1.5 to 2.0. Atom probe tomography also indicates that some NFs have complex core-shell structures.[2,14] The cores contain more, but still sub-stoichiometric, Y, while the surrounding shells are more highly enriched in Ti and O.

However, it is difficult to reconcile the SANS data with NFs that are so highly enriched in Ti that would result in much lower M/N than are observed.[12] APT results also indicate that the NFs contain large amounts of Fe (≈40 to 70%). However, the Fe is likely an APT artifact.[11,14] Varying amounts of Cr in the NFs have also been reported, in some cases enriched in a surrounding shell region,[2,14] as well as other strongly oxidizing elements like Al and V. Core-Cr shell structures have also been found in some TEM studies.[2,15,16]

Important insights on the apparent discrepancies in the character of the NFs have been provided by recent TEM studies.[11,17] There is not a single type of NF, but rather what might best be described as a zoo of NFs, even in a particular NFA like MA957. The detailed characteristics of the NFs likely vary even more from alloy to alloy, since they are very sensitive to composition and processing variables.[2,12] The following discussion will primarily focus on TEM studies of NFs extracted from MA957 on C-foils.[12] Energy dispersive x-ray spectroscopy (EDX) measurements show that NF Ti/Y ratios are close to those of the complex oxides, typically ranging from 0.5 to 1, and averaging around 0.7 to 0.8 for the larger features (8–15 nm); the nominal O/(Ti + Y) are > 1. However, the individual NFs are not stoichiometric. Smaller NFs (<8 nm) appear to have more uniform Ti/Y closer to 1. Note, there are a few exceptions with both much larger and smaller Ti/Y, These Ti/Y ratios are generally distinctly different than those measured in APT studies. Further, EDX does not find Fe in the NFs.

High-resolution TEM-Fast Fourier Transformation (HRTEM-FFT) and electron powder diffraction indexing methods can indentify diffracting NFs down to small sizes of <5 nm.[11] Some of the larger features were found to be consistent with variants of Y_2TiO_5, with various levels of reliability, depending on the plane spacing-angle indexing criteria used. The smaller features tend to be more consistent with $Y_2Ti_2O_7$. An example of a ≈5 nm probable $Y_2Ti_2O_7$ oxide is shown in Figure 5a. However, many of the NFs that could be indexed were found to be inconsistent with

any known oxide phase. A recent in foil study of a model 14CrYWT alloy reached generally similar conclusions, and was able to establish some orientation relations as well.[17]

Figure 5b shows the size distribution measured by high angle annular dark field (HAADF) TEM.[11] Consistent with other techniques, HAADF also shows that the NFs are not uniformly distributed, typically manifesting order of magnitude variations in N, and with some regions that contain few, if any, NFs. Figure 6 shows that, in addition to many isolated NFs (Figure 6a), there is a significant population of features that appear to be associated with one another (Figure 6b). The insert in Figure 6b is an APT iso-concentration image of what appears to be such an associated feature.[11] The number density of the apparently associated features is typically 5 to 10 times lower than for the isolated NFs. Note, dislocation climb may be severely restricted by the thistle-like shape of such associated features. An even lower number density of larger massively agglomerated features is also observed (Figure 6c) in MA957. While some evidence of such associated NFs has been found in in-foil TEM studies, the presence of such complex features may be an artifact of the C-extraction method, and further verification of these observations is needed. A variety of other phases found in MA957 include TiO_X and other complex precipitates containing various amounts of Ti, Al, Cr, C, N, and O. These phases also often show precipitate-precipitate associations.

In summary, there is accumulating evidence that NFs are predominantly near stoichiometric oxides, even down to small sizes. In addition to isolated NFs, morphologically complex associated precipitates may also be present in NFAs, and which may bear some functional significance. The TEM results for the extracted NFs need to be further confirmed by in-foil measurements. Other approaches to characterizing the NFs will continue to be pursued, like XRD on bulk extractions,[11,13] energy filtered TEM,[2,16,18] electron energy loss spectroscopy,[2,15] x-ray absorption spectroscopy,[19] and positron annihilation spectroscopy.[20] Finally, we note that a recent study combining SANS and small angle x-ray scattering (SAXS) in a Japanese NFA also concluded that the small NFs are $Y_2Ti_2O_7$.[21]

THE THERMAL AND MECHANICAL STABILITY OF NFs

The stability of NFs is of paramount importance. SANS studies have shown that the NFs systematically coarsen above 1,150°C, albeit with a very high effective activation energy (≈880 kJ/mole) and slow, $t^{1/5}$, time dependence.[2] More recently, long-term aging studies[2,11] have been carried out on MA967 from 850–1,000°C for times up to 19,000 h. TEM, APT and SANS studies all show that the NFs are remarkably stable, although some coarsening is observed at 1,000°C.[11] The SANS results are shown in Figure 7a–c. The corresponding changes in the grain and dislocation structures are subtle. The stability of NFAs and NFs is reflected in the softening shown in Figure 7d that is modest even at 1,000°C after more than 19,000 h.

The remarkable stability of NFAs means that they are good candidates for high temperature diffusion bonding. Another potentially attractive solid state joining method is friction stir welding (FSW). A recent APT study of a MA957 FSW[11] confirmed earlier SANS and TEM results showing that the NFs are moderately degraded by severe deformation.[2]

MECHANICAL PROPERTIES OF NFAs

As summarized in Reference 2, NFAs have remarkably high tensile, creep, and fatigue strengths. A Larson Miller plot of creep rupture data for various heats of MA957, a Japanese 12CrYWT NFA, and TMS Eurofer97 is shown in Figure 8. [2,11,22] In general, the NFAs are much stronger that the TMS alloy. The most recent results from a creep test on a French heat of MA957 that failed after 38,555 h at 800°C at 100 MPa, while a test at 825°C and 75 MPa is still running after 59,000 h.[22] The minimum creep rate measured for the 38,555 h test was $\approx 1.2 \times 10^{-11}$ s^{-1} and the total strain just prior to failure was only 0.361%.

The excellent dislocation creep properties of NFAs are controlled by an NF mediated effective threshold stress that is a large fraction of the yield stress (>0.5) (e.g., defined for tests at strain rates of $\approx 2\times10^{-3}$/s) at temperature, which results in very high effective $\varepsilon' \alpha \sigma''$ stress exponents, with n ≈ 15–35.[2,23] Schneibel and coworkers have measured creep rates in an ultrafine grained 14YWT alloy in the diffusion regime.[24] In this case, while n ≈ 1, the magnitudes of the creep rates are many orders of magnitude below those predicted for a single-phase alloy. This is attributed to suppression of grain boundary diffusion and pinning of grain boundaries.

Figure 8 shows significant MA957 heat-to-heat and NFA-to-NFA variations in the creep rupture strength.[2] The differences may be due to a combination of variations in the NFs as well as post consolidation thermal mechanical treatment mediated dislocation and grain structures. Notably, Figure 8 shows the creep strength of MA957 tubing is low in the hoop direction.

The fracture toughness of NFAs is lower in the extrusion compared to the transverse directions.[2] This has been attributed to a combination of crystallographic texturing (<110> in the extrusion direction), large grain aspect ratios (5–10), and impurity inclusion stringers. The fact that NFAs are weak in both axial (for toughness) and transverse (for creep) directions emphasize the importance of post extrusion thermal-mechanical processing treatments that result in more isotropic recrystallized microstructure and properties.[2] In principle, clean, fine grained and isotropic alloys should have better fracture toughness. However, fracture tests on HIPed alloys that contain a bimodal distribution of grain sizes showed only modest improvements in toughness. In this case the toughness appeared to be controlled by formation of cleavage microcracks facilitated by the larger grains.[2]

Consolidation at lower temperatures results in higher NFA strength and more uniform distribution of smaller grains.[18,25,26] For example, the room temperature yield strength in a series of 14YWT NFA with uniform fine (<500 nm) and more equiaxed (aspect ratios of 1–1.5) grains that was extruded at 850°C ranged from ~1,250 to 1,650

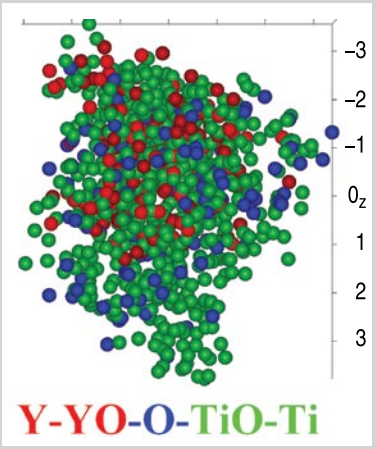

a

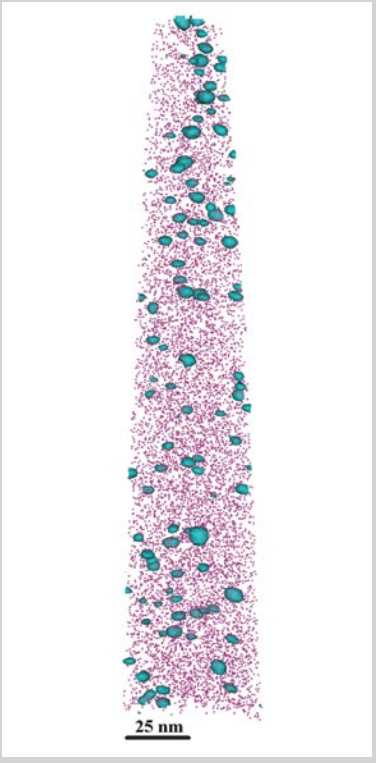

b

Figure 4. APT reconstructions: (a) an atom map of a typical Y-Ti-O NF; and (b) T + Y isocomposition contours showing the distribution of small NFs in MA957. The red Cr atoms show the shape of the needle.

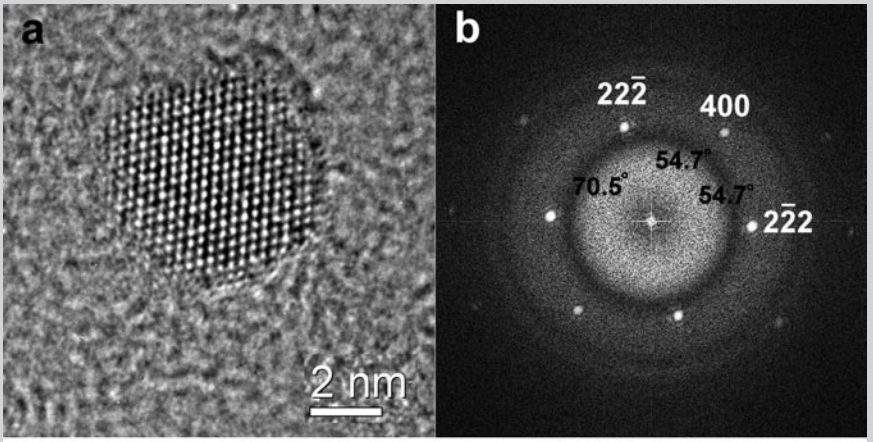

	d1{2-22}	d2{400}	d3{22-2}	angle12	angle13
measured	2.96 Å	2.60 Å	3.09 Å	53.4°	71.0°
calculated	3.06 Å	2.65 Å	3.06 Å	54.7°	70.5°

a

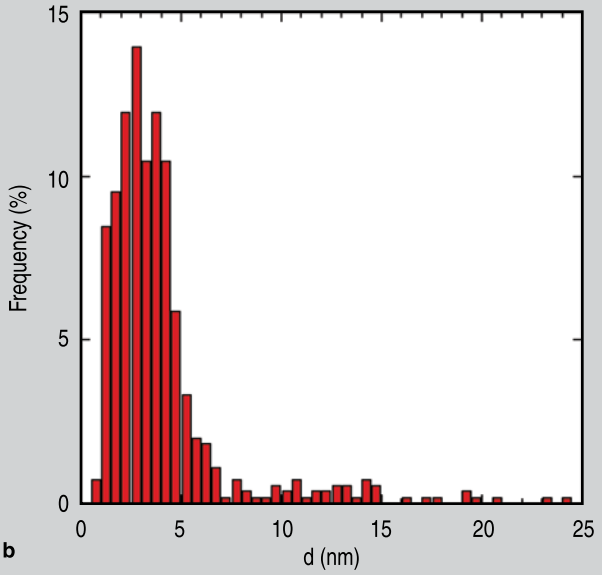

b

Figure 5. (a) HRTEM FFT indexing of a large oxide indicating it is consistent with $Y_2Ti_2O_5$; and (b) the NF size distribution in MA957 measured by HAADF.

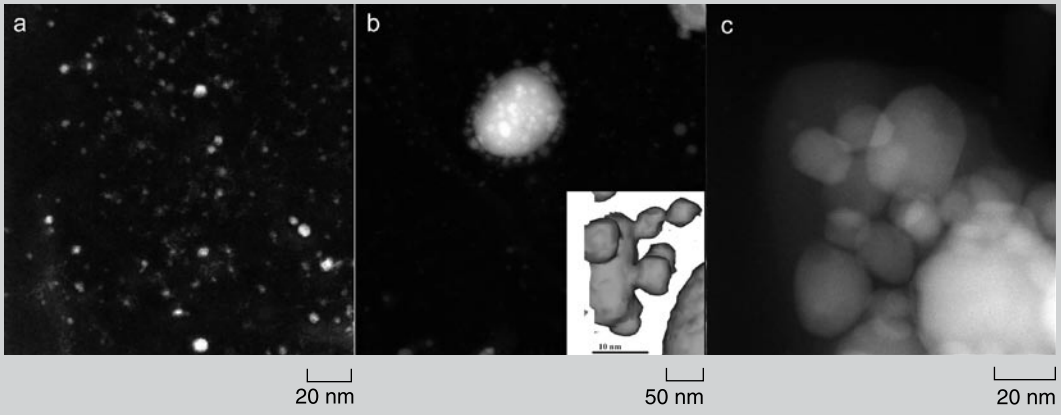

Figure 6. HAADF images showing (a) isolated NFs; (b) associated NFs and a larger precipitate including an APT image insert; and (c) larger agglomerated precipitates.

MPa. Conventional wisdom suggests that higher strength leads to lower toughness. However, the high strength NFAs processed at 850°C were found to have remarkably low transition temperatures (at 100 MPa√m), between –84 and –150°C, in the orientation when the crack propagates perpendicular to the extrusion direction (L-T).[25–27] Unfortunately, the alloy with a transition temperature of –84°C had very poor fracture toughness in the orientation where the crack propagates in the extrusion direction (T-L), with the ductile-to-brittle transition starting around 18°C and a low upper shelf toughness at slightly higher temperatures of only ≈60 MPa√m. Thus, fine and more isotropic grain structures are not, in themselves, sufficient to produce high toughness. Recent experiments also suggest that the NFA ductile tearing toughness levels are low at higher temperatures.[28,29]

TMS alloys have superior fracture properties in the unirradiated condition compared to NFA. However at high helium levels, TMS experience very severe embrittlement at lower irradiation temperatures, with maximum ductile to brittle temperature shifts estimated to be in excess of 400 to 500°C. The severe embrittlement is associated with weakening of the grain boundaries by helium, leading to a low toughness intergranular fracture.[2] High helium concentrations also produce larger increments of irradiation hardening due to bubbles.[30] In contrast low temperature helium embrittlement has not been observed in NFA. NFA also appear to suffer less irradiation hardening compared to TMS, and retain higher levels of post yield uniform elongation.[2]

MODELING

There have only been a few basic modeling studies of NFAs and NFs including ab initio calculations of the initial stages of Y-Ti-O clustering[31,32] and the bulk elastic, electronic, and energetic properties of $Y_2Ti_2O_7$ and Y_2TiO_5.[33] Lattice Monte Carlo (LMC) simulations that explored the initial stages of Y-Ti-O clustering and mapped energetically favorable NF structures, showed there is a strong chemical potential source for the formation of coherent transition phases.[2] More gener-

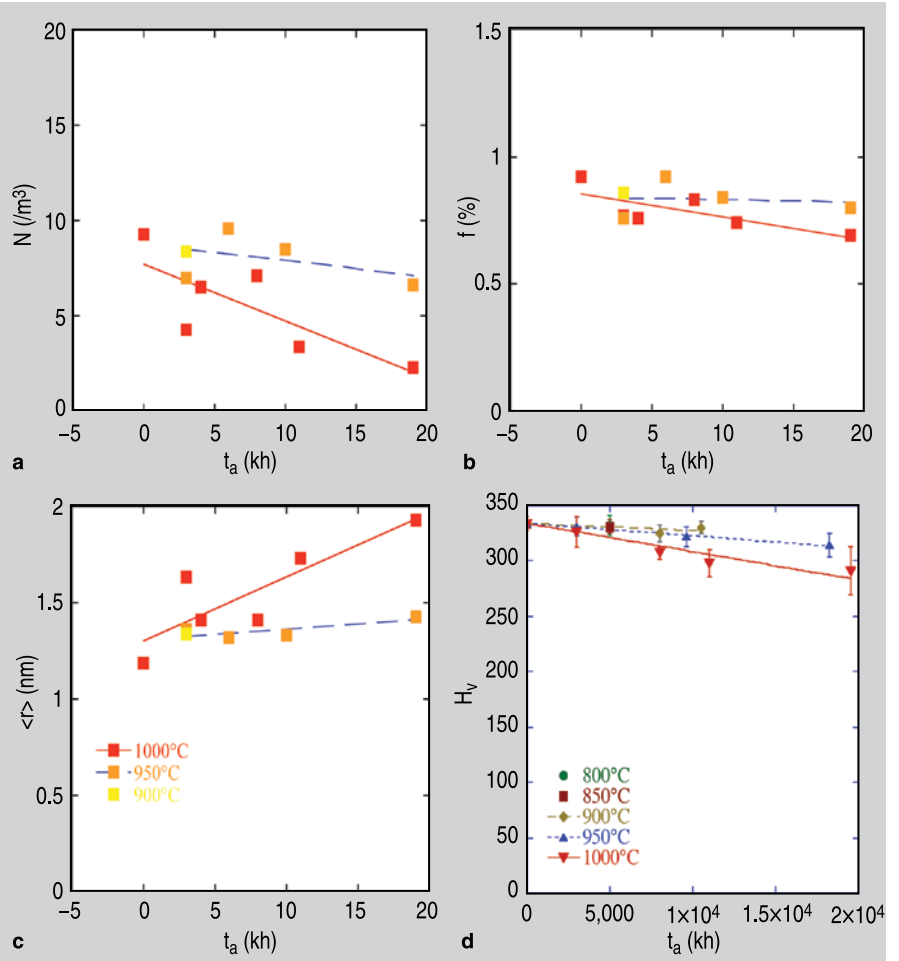

Figure 7. (a–c) SANS data on (a) NF N, (b) f, and (c) r in MA957 as a function of aging time and temperature; and (d) the corresponding microhardness as a function of time and temperature.

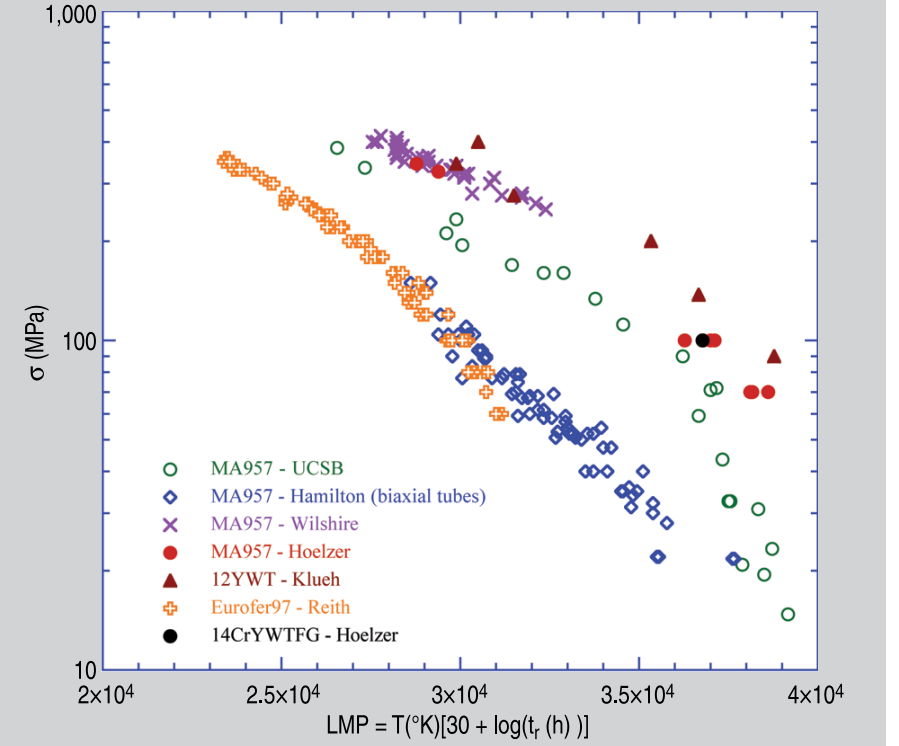

Figure 8. A Larson-Miller plot of the creep rupture time as a function of temperature and stress for various heats of MA957, along with data for a Japanese 12CrYWT NFA and a TMS Eurofer97.

ally, however, there are literally dozens of NFA and NF modeling opportunities that can be closely linked to experiment, including: (a) mechanical alloying mechanisms; (b) the thermo-kinetics of NF formation and thermal stability; (c) NF compositions, structures, interfaces and the corresponding energies; (d) dislocation-NF interaction strengthening mechanisms; (e) helium and defect-NF binding energies; and many more. Along with characterization and mechanism experiments, modeling studies of the type described above are needed to inform and parameterize multiscale models of the mechanical behavior, microstructural stability, and radiation tolerance of NFAs.

CONCLUSION

As noted in the introduction, there are many unresolved challenges facing the successful development of NFAs. These challenges also represent opportunities for materials science to make critical contributions to developing advanced fission and fusion as energy sources. In many ways, we see NFAs as providing opportunities akin to the superalloy single crystals that revolutionized jet engine and gas turbine technologies. The success of NFAs will depend on their ability to transform helium from a liability to an asset, by managing it in the form of a high number of stable nanometer-scale bubbles that have the theoretical promise of producing irradiation tolerance over a wide range of temperatures up to hundreds of dpa and thousands of appm of helium.

ACKNOWLEDGEMENTS

The University of California Santa Barbara (UCSB) and Oak Ridge National Laboratory (ORNL) research described in this article was supported by the Department of Energy Office of Fusion Energy Sciences and the Office of Nuclear Energy. Support at ORNL was also provided by the Laboratory Directed Research and Development Program. The excellent facilities for the transmission electron microscopy studies carried out at UCSBs National Science Foundation MRSEC Microstructure and Microanalysis Facility and the SANS measurements conducted by UCSB researchers at the NIST Center for Neutron Research are gratefully acknowledged. Both authors thank our UCSB and ORNL colleagues as well as our national and international collaborators and colleagues for their many contributions to the development of high performance, irradiation tolerant alloys.

References

1. S.J. Zinkle and J.T. Busby, *Materials Today,* 12-11 (2009), p. 12.
2. G.R. Odette, M.J. Alinger, and B.D. Wirth, *Ann. Rev. Mater. Res.,* 38 (2008), p. 471; and references therein.
3. G.R. Odette, P.J. Maziasz, and J.A. Spitznagel, *J. Nucl. Mat.,* 103 (1981), p. 1239.
4. L.K. Mansur and W.A. Coughlan, *J. Nucl. Mat.,* 119 (1983), pp. 1–25.
5. R.E. Stoller and G.R. Odette, *Eff. of Irrad. on Mat.: 13th Int. Sym.,* ASTM STP-955 (Philadelphia, PA: ASTM, 1987), p. 371.
6. P.J. Maziasz, *J. Nucl. Mat.,* 205 (1993), p. 118.
7. H. Trinkaus, *J. Nucl. Mat.,* 118 (1983), p. 39.
8. G.R. Odette, *J. Nucl. Mat.,* 155-157 (1988), p. 921.
9. T. Yamamoto, G.R. Odette, P. Miao, D.J. Edwards, and R.J. Kurtz, *J. Nuc. Mater.,* 386-388 (2009), p. 338.
10. G.R. Odette et al., "Helium Transport, Fate and Management in Nanostructured Ferritic Alloys: In Situ Helium Implanter Studies," *J. Nucl. Mat.,* (2010) accepted for publication.
11. G.R. Odette et al., papers to be published in *Fus. Mater. Semiann. Prog. Rept. DOE/ER-0313* (Oak Ridge, TN: Oak Ridge National Laboratory, 2010).
12. M.J. Alinger, G.R. Odette, and D.T. Hoelzer, *Acta Mater.,* 57 (2009), p. 392.
13. H. Sasasegawa et al., *J. Nucl. Mat.,* 384-2 (2009), p. 115.
14. E.A. Marquis, *App. Phys. Lett.,* 93-18 (2008), p. 181904.
15. M. Klimenkov, R. Lindau, and A. Moeslang, *J. Nucl. Mat.,* 386 (2009), p. 553.
16. S. Lozano-Perez, V. de Castro Bernal, and R.J. Nicholls, *Ultramicroscopy,* 109 (2009), p. 1217.
17. D. Bhattacharyya et al., "On the Structure and Chemistry of Complex Oxide Nanofeatures and Oxides in Nanostructured Ferritic Alloy U14YWT," to be submitted for publication in *Acta Mater.* (2010).
18. D.T. Hoelzer et al., *J. Nuc. Mat .,* 367 (2007), p. 166.
19. S. Liu, C.U. Segre, and G.R. Odette, *Trans. American Nuclear Society,* 98 (2008), p. 1067.
20. M.J. Alinger et al., *Mat. Sci. Engr. A,* 518 (2009), p. 150.
21. M. Ohnuma et al., *Acta Mater.,* 57 (2009), pp. 5571–5581.
22. D.T. Hoelzer et al., *Fus. Mater. Semiann. Prog. Rept. DOE/ER-0313/44* (2008), p. 53.
23. H. Sasasegawa et al., *J. Nucl. Mat.,* 386 (2009), p. 511.
24. J.H. Schneibel et al., *Scripta Mater.,* 61 (2009), p. 793.
25. D.A. McClintock et al., *J. Nucl. Mat.,* 386–388 (2009), p. 307.
26. D.A. McClintock et al., *J. Nucl. Mat.,* 392 (2009), p. 353.
27. D.A. McClintock et al., personal communication.
28. T.S. Byun et al., personal communication.
29. C.C. Eiselt et al., "Tensile and Fracture Toughness Properties of the Nanostructured Ferritic Oxide Dispersion Strengthened Alloy 13Cr-1W-0.3Ti-0.3Y_2O_3," *J. Nucl. Mat.* (2010) accepted.
30. T. Zong and Y. Dai, *J. Nucl. Mat.,* 398 (2009), p. 43.
31. C.L. Fu et al., *Phys. Rev Lett.,* 99-22 (2007), 225502.
32. Y. Jiang, J.R. Smith, and G.R. Odette, *Phys. Rev. B,* 79-6 (2009), 064103.
33. Y. Jiang, J.R. Smith, and G.R. Odette, *Acta Mater.,* 58 (2010), p. 1536.

G.R. Odette, professor, is with the Mechanical Engineering Department at the University of California Santa Barbara, Santa Barbara, CA 93106; (805) 893-3525; e-mail odette@engineering.ucsb.edu. D.T. Hoelzer is with Oak Ridge National Laboratory.